Ocean-Land-Atmosphere Research
A SCIENCE PARTNER JOURNAL

RESEARCH ARTICLE

Downward Mediterranean Cloudiness Beyond Little Ice Age Background Variability

Nazzareno Diodato[1], Vinay Kumar[2], and Gianni Bellocchi[1,3]*

[1]Met European Research Observatory – International Affiliates Program of the University Corporation for Atmospheric Research, Via del Pino 47, 82100 Benevento, Italy. [2]Radio and Atmospheric Physics Lab., Rajdhani College, University of Delhi, New Delhi, India. [3]Université Clermont Auvergne, INRAE, VetAgro Sup, UREP, 63000 Clermont-Ferrand, France.

*Address correspondence to: gianni.bellocchi@inrae.fr

Citation: Diodato N, Kumar V, Bellocchi G. Downward Mediterranean Cloudiness Beyond Little Ice Age Background Variability. *Ocean-Land-Atmos. Res.* 2024;3:Article 0053. https://doi.org/10.34133/olar.0053

Submitted 7 November 2023
Accepted 31 May 2024
Published 9 July 2024

Cloudiness–sea interaction substantially influences Earth's climate by shaping precipitation patterns and radiative budgets. However, our understanding of long-term variations in land-based cloud cover, spanning over decades, centuries, and more, remains limited. This study presents the most extensive reconstruction to date of the annual total cloud cover fraction across the Mediterranean, spanning 1500–2022 CE. A notable shift occurred after 1818, marked by a surge in multidecadal variability and a sustained decline in cloud cover. This change has been attributed to several factors, including the eruption of Mount Tambora in Indonesia in 1815, intensified solar forcing, and a positive phase of the Atlantic Multidecadal Oscillation. These factors collectively reshaped cloudiness beyond typical background variability. By shedding light on the complex interactions with the climate system, our findings suggest that temperature changes may drive increased cloudiness in the Mediterranean when influenced by cold air masses through advection. This emphasizes the need for a deeper exploration of the impact of clouds on regional atmospheric circulation and climate changes. Ultimately, our enhanced understanding of the relationship between cloudiness and climate change provides valuable insights for climate models. While these models consistently project a decrease in cloudiness over the Mediterranean, our findings can also be helpful in understanding cloud variability in other parts of the globe.

Introduction

Cloud cover significantly affects water cycle dynamics [1] and climate patterns [2], exerting a strong influence on Earth's energy balance, especially through marine low level formations [3]. Meanwhile, marine surfaces play a dual role. They contribute to the production of spray aerosols, which stimulate warm cloud formation by serving as condensation nuclei [4]. In addition, they influence seawater thermal anomalies through teleconnection processes, which can lead to strong stratocumulus cloud feedback [5]. Weather, clouds, and climate are some first observable phenomena that human beings experience and understand. Historical insights into these interactions date back to ancient times. Scholars such as the Hispano–Roman theologian and archbishop Isidore of Seville (560–636) recognized the complex interplay between clouds and water. Isidore even alluded to an inverse hydrological cycle model, stating that clouds draw water from the sea and winds carry sea moisture [6] (p. 277):

> The reason why the sea has no increase in its size (…) is because the clouds themselves draw up and absorb a great deal of water or because the winds carry away part of the sea, and the sun dries up part (…).

Our contemporary understanding of cloud–climate dynamics faces persistent uncertainties rooted in intricate interactions among clouds, atmospheric circulation, and the broader climate system [7]. These uncertainties arise from diverse factors, such as solar forcing, ocean dynamics [8], and aerosol-mediated radiative changes [9,10], extending to uncertainties in future climate projections [11]. The interplay between aerosols and clouds, a topic of both scientific and artistic interest, is reflected in the works of renowned artists, such as the Dutch postimpressionist painter Vincent Willem van Gogh (1853–1890) and the Norwegian expressionist and symbolist painter Edvard Munch (1863–1944), whose canvases (Fig. 1A and B) prompt contemplation of the potential influence of long-term climate shifts on the creative spirit [12].

The industrial revolution catalyzed a surge in anthropogenic aerosol emissions, especially in Western Europe, further complicating our understanding of cloud–climate dynamics. The interplay of anthropogenic aerosols with natural forces poses a challenge to historical climate modeling and the assessment of global circulation models [3]. These complexities substantially influence climate dynamics [13], with coupled feedback mechanisms playing a crucial role [14]. Recent observations of trade cumulus clouds provide a new perspective, suggesting that dynamic cloud generation may counteract the expected cloud dissipation due to global warming [15]. This insight enriches our understanding of cloud–climate interactions and prompts a reconsideration of high-climate-sensitivity model estimates.

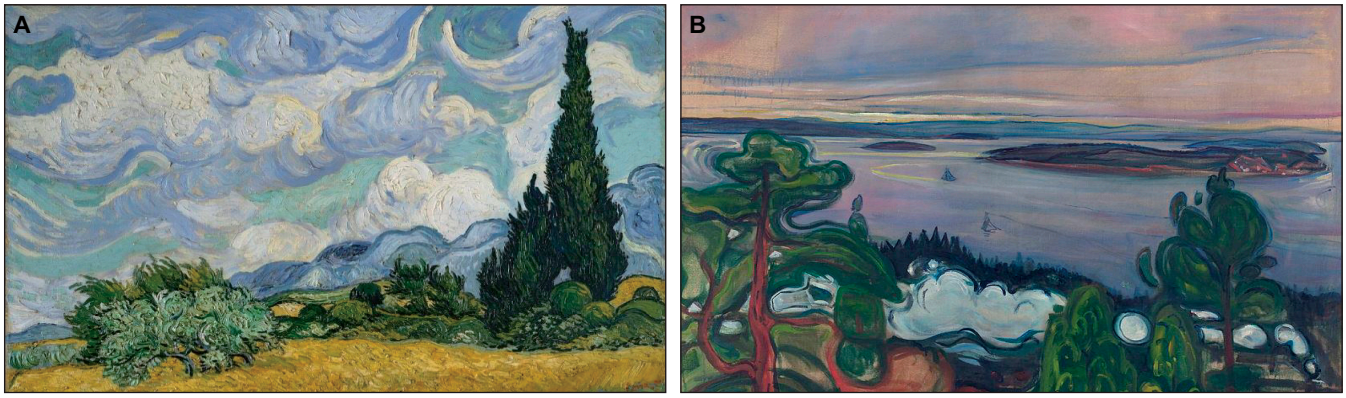

Fig. 1. Representation of distinct cloud phenomena in artistic works. (A) Vincent Willem van Gogh's painting *Wheatfield with Cypresses* (1889) depicts golden wheat fields, a towering Provençal cypress resembling a green obelisk on the right, and softer-toned green olive trees in the foreground. Colored reflections in the sky from swirling clouds, their hues possibly inspired by the changing colors of autumn or the sky's tints altered by solar refractions interacting with lingering dust from the Krakatoa volcanic eruption of 1883. However, Van Gogh himself described his painting as follows [89]: "I have a canvas of cypress trees with some ears of wheat, some poppies, a blue sky like a piece of Scotch plaid; the former painted with a thick impasto like the Monticelli's, and the wheat field in the sun, which represents the extreme heat, very thick too" (source of painting and quote: https://en.wikipedia.org/wiki/Wheat_Field_with_Cypresses). (B) Edvard Munch's artwork *Train Smoke* (1900), featuring towering trees dominating the foreground, with a lake, many islands, and the sky depicted in the central and upper regions of the canvas (source: https://fr.m.wikipedia.org/wiki/Fichier:Edvard_Munch_-_Train_Smoke_-_Google_Art_Project.jpg).

In this unique study, we focused on a detailed exploration of total cloudiness, with a specific focus on the Mediterranean region, a crossroads of interlinked climate cycles [16]. These cycles, shaped by stochastic influences from midlatitude atmospheric circulation and ocean–atmosphere interactions, such as the Atlantic Multidecadal Oscillation (AMO) [17], have a notable impact on atmospheric variability over Europe and the Mediterranean basin. In addition, variations in sea surface temperatures (SSTs) in the Pacific and Southern Oceans contribute to this intricate interplay [5,18,19], influencing cloudiness patterns and solar radiation reach [20]. Despite some incompletely understood facets of these mechanisms [21], their interplay emphasizes the need to expand our understanding of the climate-induced influences of cloudiness and their broader effects.

The history of cloudiness observations in Europe, dating back to the records of the French physician Louis Morin (1635–1715) in Paris, France, in 1665 [22], and the subsequent daily records in the Olomouc region of the present-day Czech Republic, spanning from 1693 to 1784 [23], paved the way for studies on cloudiness ranging from small-scale investigations 24–26] to broader spatial extents [13,27,28]. Some investigations focused on specific geographical areas [16,29]. For instance, Founda et al. [30] reanalyzed historical cloudiness observations spanning from 1882 to 2012 in the metropolitan area of Athens, Greece and found an increase in convective clouds during winter, along with a decline in low stratiform clouds. Matuszko and Weglarczyk [31] proposed an interesting perspective linking air temperature records in Krakow, Poland (1863–2010) to changes in cloudiness morphology. However, comprehensive field data products, particularly those focusing on the composite Mediterranean region over longer periods, including observational satellite data, remain relatively elusive [27].

In this study, we laid the groundwork for the first Mediterranean reconstruction of the total cloud cover (TCC) annual mean fraction at ground level ($TCCf_G$) for 1500 CE. This ambitious undertaking leverages hydrological and climatic factors to draw a nuanced portrait of cloud–climate interactions across different historical periods. This study aims to address the question of how total cloudiness in the Mediterranean (a "hotspot" in global climate change assessments [32]) has evolved over the past 5 centuries and how it has been influenced by natural and anthropogenic factors, bridging the gap between climate trends projected in global climate models and historical records [33]. In particular, the TCC fraction historical model [$TCCf_G$(H)] aims to overcome the limitations of complex models through parsimony. Relying on simplified inputs, including pivotal forcing indicators and regional climate factors, this model assesses the annual mean fraction of TCC based on ground observations from the CRU TS (Climatic Research Unit Time Series) v4.04 network ($TCCf_G$), culminating in the generation of an extensive time series dataset (1500–2022 CE) spanning distinct climate periods: the central Little Ice Age (LIA; 1500–1715), the end of the LIA (1716–1849), and the Modern Warming Era (MWE; 1850–2022).

Materials and Methods

Experimental design

The unique geography and history of the Mediterranean make this region of scientific interest. A Mediterranean climate is characterized by mild, wet winters and warm to hot, dry summers, typically found on the western side of continents at low to midlatitudes. What sets the Mediterranean region apart is the presence of a significant body of water. The Mediterranean Sea, lying on the western edge of a broad geographical expanse, is a semienclosed sea bordered by the Euro–Asiatic continent to the north and east and Africa to the south. However, the temporal and spatial dynamics of regional components influenced by these large-scale forces are intricate. The interplay of orography and land–sea distribution plays a pivotal role in shaping basin-scale climate patterns and their connection to global trends [34]. The Mediterranean, a geographical confluence par excellence, holds considerable significance for the global climate system (Fig. 2A).

Distinguished by its unique climate dynamics, the Mediterranean region emerges as a pivotal crossroads where Europe, Asia, and Africa converge. Beyond its geographical relevance, the Mediterranean holds dual roles: as a source of moisture for cloud formation and precipitation and as an arena of intricate

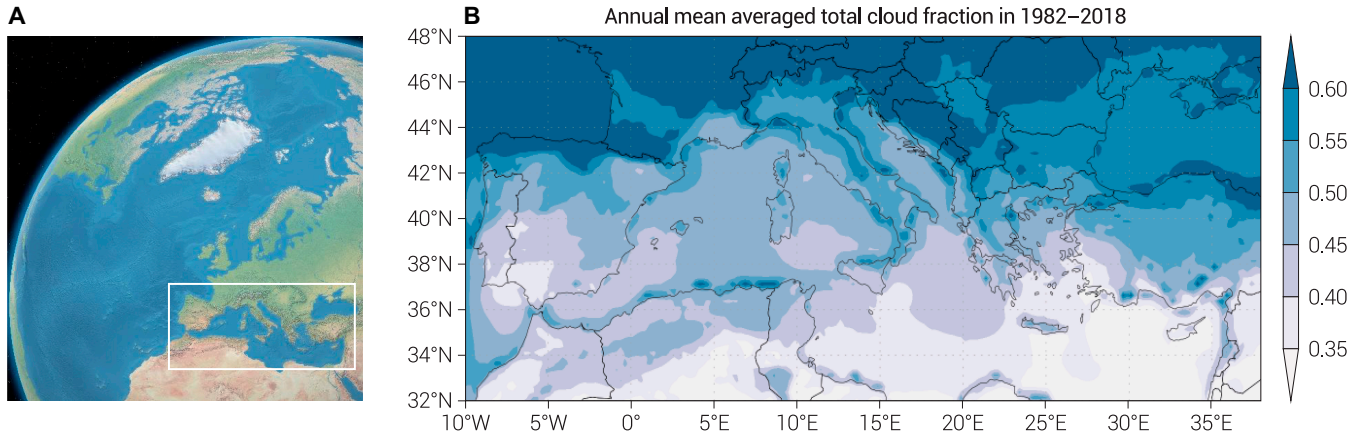

Fig. 2. Study area and TCC fraction in the Mediterranean (1982–2018). (A) Geographical setting of the Mediterranean area (white square), generated using the Natural Earth II free domain dataset (http://www.shadedrelief.com/natural2/globes.html). (B) TCC annual areal mean fraction over the Mediterranean derived from EUMETSAT CM-SAF data with a spatial resolution of 0.25° km. This dataset spans the period from 1982 to 2018 and is sourced from Climate Explorer (http://climexp.knmi.nl).

land–sea interplays and seasonal fluctuations, underscored by amplified climatic shifts [35]. Within this mosaic, the formation of cloud cover patterns takes shape through an interplay of regional-scale influences, ranging from atmospheric circulation to ocean–atmosphere interactions and air mass origins [36]. Notably, the spatial distribution of the annual mean fraction of TCC ($TCCf_S$) across the Mediterranean, captured through sequences of EUMETSAT (European Organisation for the Exploitation of Meteorological Satellites) CM-SAF (Satellite Application Facility on Climate Monitoring) data from 1982 to 2018 at a resolution of 0.25° km, highlights a panorama of uniformity and dynamism (Fig. 2B).

Areas such as the eastern Mediterranean, the northern fringes of Spain with the Pyrenees Mountains, the Italian Apennine region, and the Adriatic coastline appear as cloud havens, with $TCCf_S$ values around 0.60. Substantial stretches of the central and southern Mediterranean expanse, including Portugal and various coastal stretches, even extending to Northern Africa, feature $TCCf_S$ values below 0.50. However, parts of Africa and the southern seas even record lower $TCCf_S$ values of less than 0.40.

We compiled a consistent dataset spanning 1935–2000 enriched with specific variables, including summer precipitation (P_{sum}) [37], seasonal temperature (T_{seas}) [38], Palmer drought severity index (PDSI) [39], AMO [40], and $TCCf_G$ (CRU TS 4.06 land 0.50°) [41]. Higher-resolution satellite-derived $TCCf_S$ (EUMETSAT 0.25°) data from 1982 to 2018 were also included. All datasets were accessed through Climate Explorer (http://climexp.knmi.nl). To ensure up-to-date information, data were extended until 2022 using Climate Explorer, specifically using GPCC (Global Precipitation Climatology Centre) v2020 data (0.25° resolution) for precipitation, E-OBS (ENSEMBLES OBServation) (Europe, 0.25° resolution) for temperature, CRU self-calibrating (0.5° Global 4.0) for PDSI, and HadSST (Hadley Centre Sea Surface Temperature Dataset) version 4 for AMO (0° to 60°N, 0° to 80°W minus SST 60°S to 60°N), with attention paid to verifying homogeneity between the 2 time series.

We used web-based tools, including STATGRAPHICS (http://www.statpoint.net/default.aspx), WESSA (https://www.wessa.net/tsa.wasp), CurveExpert Professional 1.6 (https://www.curveexpert.net), and AnClim (http://www.climahom.eu/software-solution/anclim), for time series analysis and homogenization [42].

Statistical historical model, $TCCf_G(H)$

The cloudiness response to climatic factors often reflects the influence of regional-scale climate dynamics. Positive anomalies in the TCC fraction over the Mediterranean region ($TCCf_G$) are the outcomes of increased rainfall (P_{sum}) as determined by the modified variation coefficient (MVC) and elevated PDSI. Similarly, $TCCf_G$ is subject to larger-scale climate resonances, with negative (positive) phases of the AMO corresponding to below (above) normal cloudiness climatological means. Guided by these considerations, historical cloudiness estimation (expressed as a fraction of TCC) was developed using a multivariate regression model tailored to the Mediterranean region. On the basis of Wilby et al. [43], the initial step of the $TCCf_G$ model, which used predictors in a multiple regression model (MRM), was as follows:

$$TCCf_G(\mathrm{MRM}) = \sum_{j=1}^{n} \beta_j \cdot p_{ji} + \beta_0 + e_i \quad (1)$$

where $TCCf_G(H)$ represents the TCC annual mean fraction, p_{ji} represents the predictors, n is the number of predictors, β represents model parameters, and e_i denotes the modeling error. By solving Eq. 1 and expanding it, we derive the formulation for the $TCCf_G(H)$ historical model, which follows the following structure:

$$TCCf_G(H) = \alpha \cdot P_{sum} \cdot \mathrm{MVC} + \varphi \cdot \mathrm{PDSI} + \gamma \cdot \mathrm{AMO} + \eta \cdot T_m + B \quad (2)$$

Here, MVC is calculated as follows:

$$\mathrm{MVC} = \frac{\mathrm{SD}\left(T_{seas}\right)^{-\vartheta}}{\mathrm{Mean}\left(T_{seas}\right)^{-\kappa}} \quad (3)$$

where T_{seas} represents the seasonal mean temperature (°C). This approach allows factors such as precipitation and interseasonal temperature variations (P_{sum} and MVC) to play a significant role in cloudiness changes, even during years with lower overall precipitation.

The PDSI term captures the positive (negative) shift in soil water deficit from wet (dry) years (or vice versa), which then influences cloud cover changes through the water cycle, as represented by the PDSI term. This process involves the transfer of information from the surface to cloud formation.

The sequence of processes that contribute to the propagation of the $TCCf_G(H)$ signal, as described in Eq. 3, illustrates how

the cloudiness signal evolves through different aspects of the hydrological cycle using various predictors: P_{sum} (summer precipitation), MVC (interseasonal temperature range), PDSI (latent heat), AMO (atmospheric circulation), and temperature (sensible heat). While we previously explained and mapped the relationship between some predictors and cloud cover, our focus now shifts to the mean annual temperature and the product term P_{sum}·MVC. Groisman et al. [44] developed an approach that considers the overall effect of clouds on various meteorological variables over Northern Hemisphere land areas, including surface air temperature, atmospheric pressure, air humidity, and wind characteristics. Cloud cover has a significant impact on temperature because it influences the balance between incoming (short-wave) solar radiation (which is reflected and absorbed) and outgoing infrared (long-wave) radiation.

Results and Discussion

Model evaluation

The TCC data were sourced from CRU TS 4.06 (land) for model calibration and validation, providing actual $TCCf_G$ values at a spatial resolution of 0.5°. This dataset version has maintained consistent availability since 1935, making it suitable for calibration (1935–1980) and subsequent validation (1981–2021). The 46-year calibration dataset exhibited a highly significant linear relationship ($y = a + b{\cdot}x$) between actual (y) and predicted (x) data (F test, $P \sim 0.00$, $R^2 = 0.68$). This robust relationship is visually represented in the scatterplot in Fig. 3A.

The calibration yielded a slope (b) of 1.006 (±0.103 SE) with an intercept (a) of 0.003 (±0.050 SE). Merely 2 data points (occurring in 1972 and 1979) fell beyond the 95% prediction bounds for new observations (Fig. 3A, light pink band).

Further corroborating the accuracy of the calibration, the mean absolute error (MAE) of 0.006 was smaller than the SE of the estimates (0.009), with a modeling efficiency (EF) (Nash–Sutcliffe EF coefficient) above 0.60 (EF = 0.64) indicating limited model uncertainty. The congruence between the actual and model-predicted data distributions was confirmed by the Kolmogorov–Smirnov (K–S) test, indicating a high likelihood that both data samples (actual and modeled) originated from the same distribution. The maximum distance (DN) between the 2 distributions was 0.13, with a K–S statistic of 0.63 and an approximate P value of 0.83. The distribution of model residuals, as shown in Fig. 3B, exhibited Gaussian-like characteristics with no skewness. Notably, the residuals did not demonstrate any evidence of serial autocorrelation, as evidenced by the Durbin–Watson (DW) statistic of 1.56 ($P = 0.05$). The DN between the 2 distributions was 0.13, with a K–S statistic of 0.63 and an approximate P value of 0.83.

The validation phase extended from 1981 to 2021, as depicted in Fig. 3C, revealed a consistent alignment of trends between actual data (shown by the blue line) and predicted data (indicated by the orange line) within this validation time frame. In this way, the validation revealed a statistically significant linear relationship between the actual and projected data (F test, $P \sim 0.00$, $r = 0.69$). Similarly, the MAE of 0.008 was smaller than the SE of the estimates (equal to 0.011), with an EF of 0.45. Furthermore, the DW statistic (DW = 2.09, $P = 0.57$) confirmed the absence of serial autocorrelation in the residuals. Moreover, the P value of 0.59 indicated no statistically significant difference between the 2 distributions at the 95% confidence level for the K–S test (DN = 0.17, K–S = 0.77).

In addition, supplementary validation was conducted to assess the performance of $TTCf$ at a spatial scale smaller than that for which the model was initially developed. This extended validation involved comparing the model's estimates with cloud cover data from Louis Morin's observations in Paris from 1665 to 1713, as provided by Pliemon et al. [22]. This particular validation constituted a central test of the model's effectiveness for historical reconstruction. As shown in Fig. 3D, a statistically significant relationship exists between the modeled $TCCf_G$(H) values and TCC (in octas), with F test, $P < 0.05$ and $r = 0.61$ (MAE = 0.71, EF = 0.38). In addition, the K–S test revealed no statistically significant difference between the 2 distributions

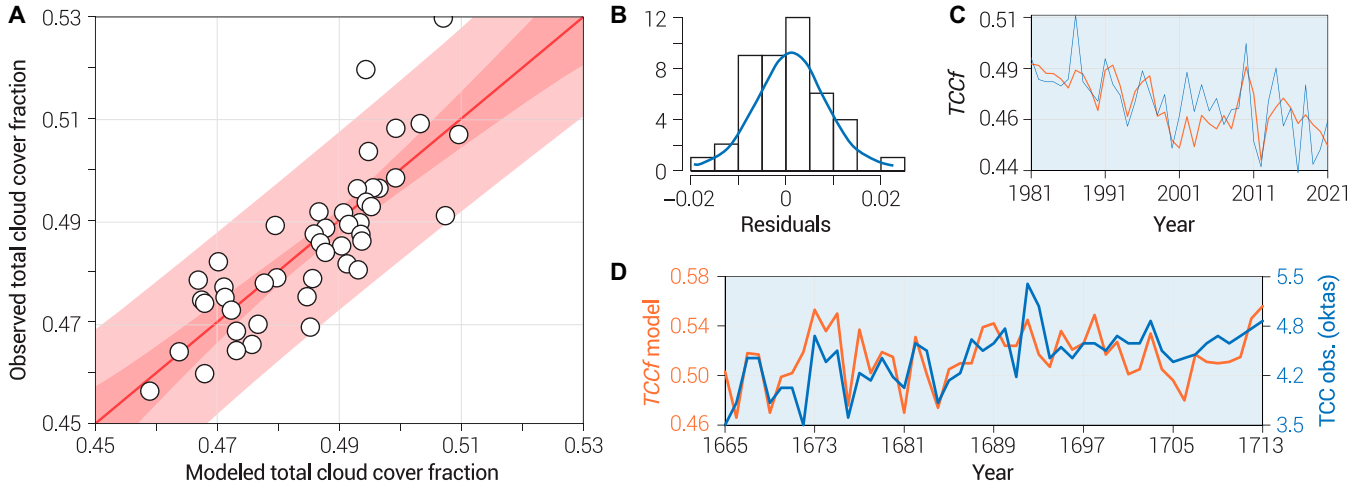

Fig. 3. Calibration and validation of the TCC fraction model in the Mediterranean area. (A) Scatterplot comparing the modeled (Eq. 1) and observed TCC annual mean fractions during the calibration phase over the period 1935–1980. The inner bounds show 90% confidence limits (power pink shade), whereas the outer bounds display 95% prediction limits for new observations (light pink shace). (B) Histogram of residuals along with their fitted normal distribution (blue line). (C) Coevolution of the modeled TCC fraction (represented by the orange line) and the observed TCC fraction (indicated by the blue line) during the validation period 1981–2021. (D) Coevolution between the modeled Eq. 2 and the observed data for the TCC annual mean fraction at Louis Morin's Observatory in Paris (France) during the historical validation period 1665–1713. The data generated and analyzed in this model assessment are available in Table S1.

(DN = 0.22, 2-sided large sample K–S statistic = 1.11, $P = 0.17$). On the basis of these analyses, we propose that the $TCCf_G$(H) model can be effectively used.

The parameters of Eq. 2 were determined as $\alpha = 0.0002$ (± 0.0002), $\varphi = 0.007$ (± 0.0020), $\gamma = -0.04$ (± 0.0112), and $\eta = -0.01$ (± 0.0041), which act as proportional criteria, adjusting the cloud cover fraction based on the annual variations of the climatic predictors, and $B = 0.602$ represents the cloud cover baseline. In addition, the 2 parameters $\vartheta = -0.50$ and $\kappa = -0.20$ in Eq. 3 modulate the effect of summer precipitation (P_{sum}).

To evaluate the relative influence of each climatic predictor on the cloud fraction, we analyzed the calibration dataset using the standardized coefficients (α', φ', γ', and η') of Eq. 2, which were obtained by dividing the estimated values of the regression coefficients by their respective SEs, which served as a valuable metric to assess the contribution of each predictor to the cloud cover fraction. These coefficients consider the relative scales of the predictors, facilitating a direct comparison of the influence of different climatic factors. Specifically, AMO ($\gamma' = -3.58$) and PDSI ($\varphi' = 3.54$) emerge as the most influential factors on cloud cover. Close behind is T_m ($\eta' = -2.43$), with negative effects like AMO, followed by the combined effect of P_{sum} and MVC ($\alpha' = 1.16$). This analysis supports the deliberate selection of the specific input factors of Eq. 2, highlighting their central role as key drivers influencing the dynamics of Mediterranean cloudiness. In our interpretation, the influence of temperature and moisture transport (including the position and strength of high- and low-pressure systems) on cloud formation is reflected in the pronounced importance of SST anomalies occurring in the North Atlantic in shaping Mediterranean cloudiness dynamics. This influence of the AMO is primarily combined with that of the PDSI, representing a key aspect of the hydrological cycle and aligning with the latter's critical role in either generating or suppressing cloud formation. Following this, T_m and the P_{sum}·MVC product enter Eq. 2 and influence cloudiness at distinct spatial scales. Indeed, the annual mean cloudiness, as a large-scale variable, logically exhibits a reduced dependence on these 2 inputs, which play a more pronounced role at local scales.

Temporal relationship between regional-scale climatic factors and cloudiness

The influence of clouds on temperature is shaped by a delicate interplay between 2 opposing effects: cooling due to lowered solar radiation and warming caused by diminished outgoing long-wave radiation [45]. This intricate balance is further complicated by local positive feedback loops between surface warming and decreased cloud cover [46]. In addition, a reduction in the occurrence of stratiform clouds, which is likely linked to rising temperatures rather than diminished water vapor content in the air, adds to this complexity [47]. To simplify this relationship, we propose an empirical approach to quantifying the reduction in the TCC in relation to the increase in the mean annual surface temperature. Specifically, in Eq. 2, the temperature input (T_m) is assigned a negative coefficient, which is in line with the advocacy of Mendoza et al. [20], who established that higher temperatures correspond to decreased cloud cover. Figure 4A shows a statistically significant relationship [as evidenced by a P value in the analysis of variance (ANOVA) less than 0.05] between T_m and $TCCf_G$ at a 95% confidence level.

Only 3 data observations fell beyond the 95% predicted boundaries (Fig. 4A, light pink band). A negative correlation ($r = -0.42$) was observed. This correlation coefficient was comparable to that obtained by Mendoza et al. [20], which was equal to −0.54. Nonetheless, this discrepancy may have stemmed from the distinction between surface and tropospheric temperature changes, a factor accounted for by Mendoza et al. [20]. In addition, variations in the TCC dataset and the analyzed years could account for differences in correlation strength. Notably, the correlation between temperature (mean, maximum, and minimum) and TCC exhibited the strongest association with annual maximum temperature [45]. However, it should be acknowledged that the temperature dataset used for the $TCCf_G$ model only provided information about the mean temperature.

Rising temperatures trigger an increase in evapotranspiration, a phenomenon linked to global trends of heightened cloud cover and precipitation patterns [48]. During wet summer spells, annual cloudiness tends to be higher than that during dry summer spells. This behavior was mirrored by the smaller

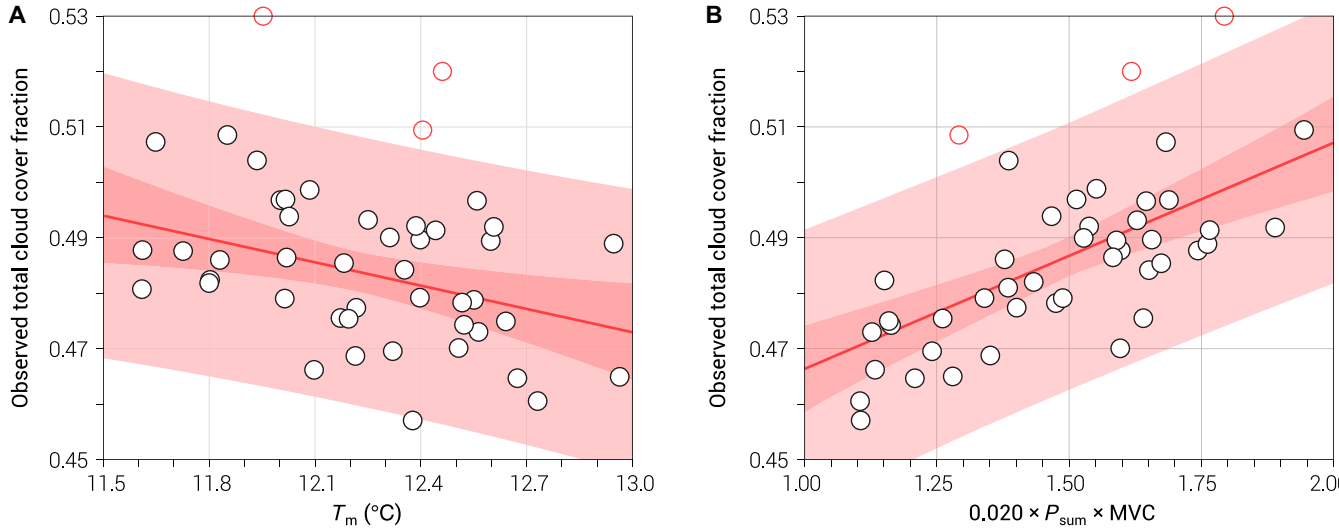

Fig. 4. Scatterplots illustrating the relationships between regional-scale climatic factors and cloudiness in the Mediterranean area from 1935 to 1980. (A) Correlation between the mean annual temperature and TCC fraction (CRU TS 4.06 land 0.50°). (B) Correlation between the product of summer rainfall (P_{sum}) and the MVC and TCC fraction.

interseasonal temperature range, represented by MVC, which dampened temperature jumps by fostering increased cloud cover and vice versa. Notably, the positive correlation observed in MVC mirrored that observed in precipitation. However, the related exponents (ϑ and κ) were negative because the rise in MVC inversely corresponded to the increase in cloud cover. This was rooted in the experimental concept that a higher intraseasonal temperature range leads to reduced cloudiness because cloudier skies tend to maintain temperatures within a narrower range of extremes. Ultimately, the product P_{sum}·MVC, as expressed in Eq. 2, yielded a stronger correlation with cloud cover than if these factors were considered individually in the model. The scatterplot in Fig. 4B depicts a statistically significant relationship (indicated by $P < 0.05$ in the ANOVA) between this product (P_{sum}·MVC) and $TCCf_G$, with $r = 0.70$ indicating a moderately robust relationship between these 2 variables. The MAE of 0.009 was smaller than the SE of the estimates, which was 0.012. Similarly, only 3 data points fell outside the 95% predicted boundaries (Fig. 4B, light pink band).

Spatial correlation among precipitation, drought, oceanic influences, and cloud cover

We used global slope regression to infer long-term variations in convective and low cloud cover by analyzing historical patterns in precipitation extremes from Global Precipitation Climatology Project data [49]. A similar observation was made by Cox et al. [50], who revealed that expanded land areas experiencing intensified daytime warmth correlated with an increase in cloud cover, specific humidity, and precipitation. Notably, moisture-related factors such as relative humidity and precipitation have been identified as influential climatic factors controlling cloud cover in the China region [13]. Although these drivers persist throughout the year, their impact is particularly pronounced during the warm season, particularly within the Mediterranean region. Given that summer primarily dictates the interannual variability of cloudiness, as other seasons are inherently cloudier, a robust correlation emerges between P_{sum} and $TCCf_G$, surpassing the correlation with annual precipitation. Thus, the positive spatial correlation between cloudiness and precipitation also holds true for the Mediterranean region. In particular, a significant correlation was observed between P_{sum} and the annual *CCTf* CRU TS 4.06 grid data, with a higher spatial correlation observed in the central Mediterranean sector, where $r > 0.5$ (Fig. 5A).

Regarding this term, Richards and Arkin [51] corroborated the positive coefficient observed in the Mediterranean region. They suggested that the correlation between estimated rainfall and mean fractional cloud coverage for a specific area strengthened as spatial and temporal averaging increased. Precipitation also contributed to convection by providing sea moisture and facilitating evapotranspiration, leading to the redistribution of moisture toward the mainland. Increases in Mediterranean temperatures play an important role in moisture transfer and the enhancement of cloud cover [20]. These temperature changes affect not only the sensible heat exchange between the sea, land, and atmosphere but also the water vapor evapotranspiration from water bodies and vegetation surfaces. Consequently, the atmospheric radiation heating rate is modified, which, in turn, influences humidity, cloud formation, and precipitation patterns [52]. In this context, rainfall positively affects the PDSI input data of the $TCCf_G$(H) model, as an increase or decrease in precipitation usually translates into an increase or decrease in soil moisture [53]. Affecting the PDSI, changes in precipitation levers have implications for the water cycle as variations in soil moisture influence the return of water to the atmosphere through evaporation, subsequently affecting cloud formation.

These intricate interactions are also reflected in the Mediterranean region, where cloud cover changes are influenced by PDSI and the associated water cycle. Notably, the correlation between PDSI and $TCCf_G$ was prominent across the northern Mediterranean, with $r \sim 0.60$, whereas the correlation was weaker in the southern areas (Fig. 5B). Previous research demonstrated the significance of the AMO as a large-scale driving force for the interannual *TCCf* variability in the Mediterranean region because of its influence on the surface air temperature of the Northern Hemisphere [54]. The findings of Markonis et al. [55] further supported the assertion that atmospheric circulation significantly affects Europe's climate, leading to potential fluctuations in cloud cover.

TCC fraction historical reconstruction

Using Eq. 2, $TCCf_G$ was reconstructed (mean annual values averaged across the Mediterranean) for 3 periods, with values of 0.50 ± 0.010 for 1500–1715 and 1716–1849 and 0.49 ± 0.016

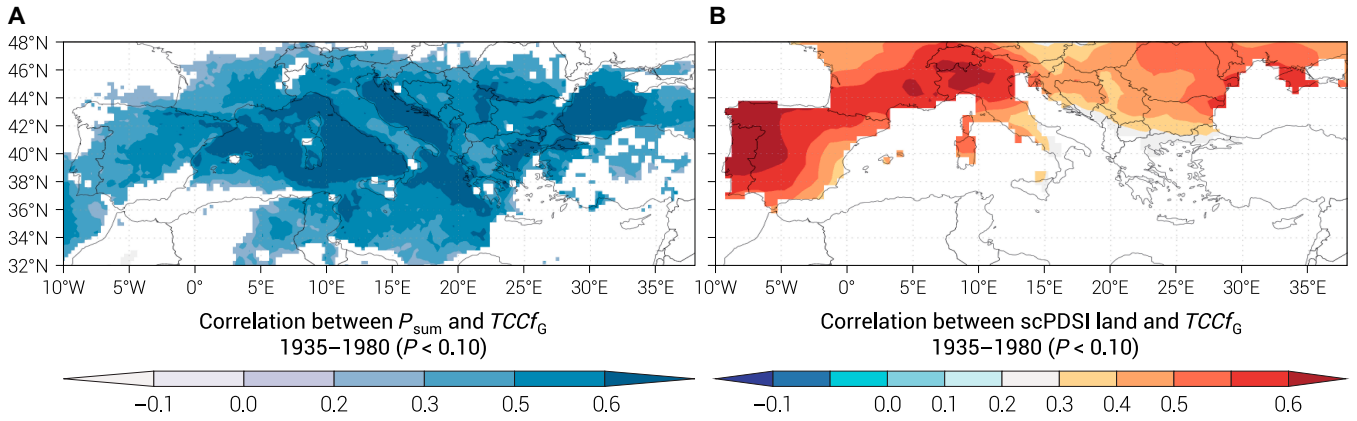

Fig. 5. Correlation analysis of summer rainfall, drought severity, and total cloud fraction. (A) Correlation coefficient between the time series of summer rainfall from GPCC v2020 analysis 0.5° resolution [90] and the spatial pattern of TCC. (B) Correlation between the time series of summer self-calibrated PDSI (scPDSI; data from Cook et al. [39]) and TCC field, covering the calibration period of 1935–1980. The TCC data were obtained from CRU TS 4.06 (maps arranged using Climate Explorer, http://www.climexp.knmi.nl).

for 1850–2022 (Fig. 6D). These variations in the reconstructed $TCCf_G$ offer a mosaic that mirrors large-scale circulation patterns. However, this relationship has not been uniformly constant over time, and its stability has been affected primarily by atmospheric processes manifested in the Mediterranean, driven by temperature and the water cycle. Our study reveals that these historical variations reflect climatic rhythms shaped by multifaceted factors, most notably the influences of the end of the central and later LIA, which coincide with the longest cold spells within our analyzed period (Fig. 6C). The cloudiness was intertwined with the oscillations of the AMO and the cadence of solar activity, accompanied by predominantly negative or neutral phases of the AMO (Fig. 6F, green line), as well as a low level of sunspot activity (Fig. 6G, red line). The first period unfolded as a relatively stationary cloud cover pattern with occasional fluctuations. After a few decades, there was a notable increase, echoing the rise of low clouds across Europe after 1550, followed by a subsequent decline after 1850 [56]. From 1600 onward, cloudiness embarked on a gradual descent, persisting throughout much of the 18th century until the early 19th century. However, this descent was occasionally interrupted by small phases of recovery. One such significant phase was the cold period during the Late Maunder Minimum (LMM), which spanned from 1680 to 1715 (blue vertical band in Fig. 6D). This period elucidates the relationship between temperature fluctuations and cloud cover variations in the Mediterranean region.

To further explore the above relationship, we performed an empirical orthogonal function (EOF) analysis. This technique involves breaking down the continuous space–time field into a series of orthogonal spatial patterns and their associated uncorrelated time series, commonly referred to as principal components. EOF analysis is widely used in climate model evaluation (e.g., 57]). Specifically, we created a reconstruction of the first EOF, which explained the largest proportion of variance (44%). This reconstruction was based on the atmospheric pressure field in Europe from 1680 to 1715 (Fig. 7B). This pattern bears some similarities to the map depicted in Fig. 7A, which illustrates the difference in 500-hPa geopotential height (in meters) between the final steady state and the time mean of years 1 to 100 of the synchronously coupled experiment for the incipient glacial climate (final minus initial). The 2 maps outline a substantial reduction in precipitation over the Fennoscandian region (across Sweden, Finland, and Russia), likely due to cold air advection. At the same time, anomalous cyclonic circulations are responsible for increased cloudiness and cooler conditions across southern Europe [58]. This correlation further corroborates previous research using NCEP/NCAR (National Centers for Environmental Prediction/National Center for Atmospheric Research) reanalysis data [59]. Specifically focusing on the Mediterranean, Trigo et al. [59] identified heightened storm activity in the region, which was thought to be associated with amplified cloud cover during episodes of winter blocking. Nonetheless, even before the LMM, when the climate was even colder (between the late 1500s and the late 1600s) (Fig. 6E), the mean cloud cover remained consistently above its long-term mean (Fig. 6D). However, with the onset of the LMM, a multidecadal decline in $TCCf_G$ over the Mediterranean region became notably pronounced, especially since the beginning of the 18th century (Fig. 6C, ocher line), consistent with Morin's observations on cloud movement and their interdecadal variability from 1665 to 1713 [22], indicating reduced westward air movement during winter.

The end of the 18th century was marked by a period of remarkably low cloud cover (Fig. 6D, blue line), which was congruent with the megadrought observed over north–central Europe from 1779 to 1827 CE [60]. Similar patterns of recurrent and moderate drought periods in the western [61] and central [62] Mediterranean further reinforce this historical timeline. During this period, an intriguing phenomenon emerged in the depictions of summer skies until the early 19th century. Artists of the time often captured cloud cover ranging from 50% to 75% in their works [56]. The culmination of the late LIA was denoted by an extreme cloudiness value of 0.53 in 1814. Intriguingly, during this first period, $TCCf_G$ displayed a slight decreasing trend (Fig. 6D, blue line).

This trend echoed observations made for northern Fennoscandia (across Finland, Norway and Sweden) [63]. The 19th century was also marked by the eruption of Mount Tambora (Indonesia) in 1815, an event that triggered a crescendo in the $TCCf_G$. Following the eruption of Mount Tambora in 1815 (Fig. 6D, black dot) and the subsequent year (1816), the time series demonstrates a noticeable second peak in $TCCf_G$. Our study, drawing parallels with reanalysis and satellite-based machine learning studies, underscored the legacy of this eruption: an approximate 10% rise in cloud cover [3], entwined with positive PDSI anomalies (Fig. 6A and B). It is at this juncture that our study charted an unprecedented course, identifying a change point in 1818 (Fig. 6C, red arrow), a point of departure that reconfigured multidecadal variability, heralding an irreversible decline in cloudiness (Fig. 6D). This shift in cloud cover reflected the decrease in cloudiness evident in the post-1850 Neuberger painting sample (in Germany) [56]. In addition, its variability demonstrated uninterrupted growth, surging beyond the background of the LIA (Fig. 6C). Specifically, the reduction in cloudiness exhibited statistical significance with a decreasing Mann–Kendall test trend (S: −807, Z: 8.66, $P \sim 0.00$), whereas the enhancement of its variability displayed significance with an increasing trend (S: 748, Z: 8.41, $P \sim 0.00$). This divergence corresponded to an initial gradual increase in AMO and solar activity. Subsequently, with the advent of the 20th century, the AMO surged into a positive phase (Fig. 6F), accompanied by a significant rise in solar forcing (Fig. 6F) and temperatures (Fig. 6E). This combination of factors likely contributed to a substantial decrease in cloud cover in the Mediterranean area during the MWE. This phenomenon is evident through the interpolation of the annual $TCCf_G$ data with a third-order polynomial line (Fig. 6D, line with small blue dots). This profound interaction, especially evident after the 1818 change point, was a hallmark of our study and echoed similar findings [64], indicating the dominant roles of external forces—volcanic, solar, and oceanic—in their mutual influence after the LIA.

As the 20th century unfolded, a crescendo of influences emerged, shaping cloud cover across the Mediterranean. These forces not only shaped cloud cover across the entire Mediterranean expanse but also imprinted their signature on specific locales. The mean $TCCf_G$, averaged by our model for the Mediterranean warming era, aligned with historical cloudiness assessments for Greece from 1882 to 2012 [30], which observed a reduction in stratiform low clouds during winter. Moreover, the accelerated trend of $TCCf_G$ in recent decades concurred with the data reported for Montenegro (Balkan peninsula) [65], as well as with negative trends indicated for the Chinese mainland [66]. In addition, Sfîcă et al. [67] supported a similar negative trend across Europe, attributing this decline to an increase in circulation types related to the establishment of high-pressure centers in the central and northern parts of the European continent. In particular,

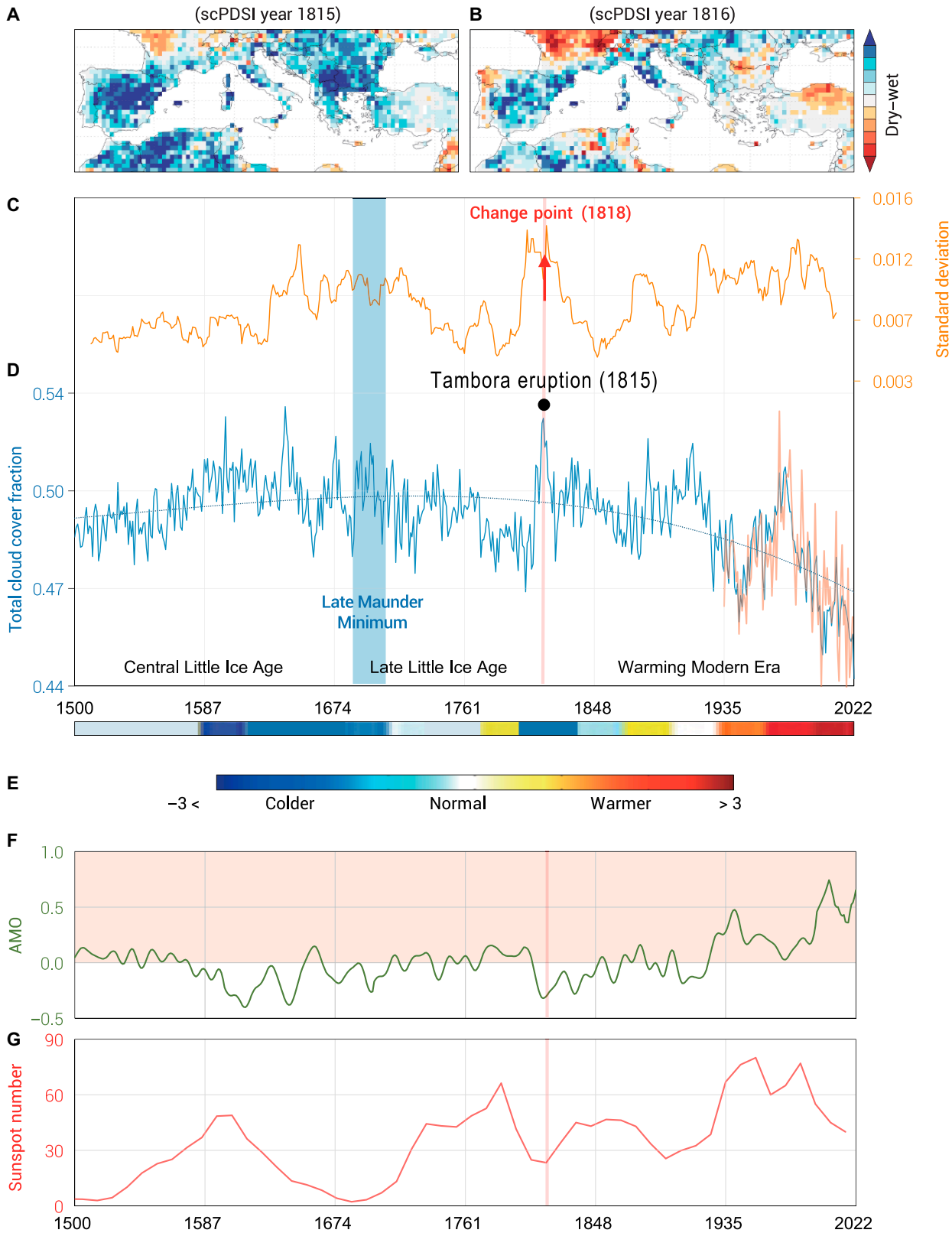

Fig. 6. Evolution of cloudiness and large-scale climate forcing in the Mediterranean region (1500–2022 CE). (A) Map illustrating PDSI anomalies compared with the 1961–1990 mean for the year 1815. (B) Map illustrating PDSI anomalies compared with the 1961–1990 mean for the year 1816 {(A) and (B) based on data from Cook et al. [39]}. (C) Multidecadal variability using a 21-year moving window standard deviation of $TCCf_G$ values (ocher line), with a notable change point in the year 1818 (arrow red), identified through the double-shift standard normal homogeneity test developed by Alexandersson and Moberg [91]. (D) Annual reconstructed $TCCf_G$ (1500–2022 CE) values (blue line), overlaid with observed $TCCf_G$ (1935–2022) values (orange line). (E) Surface air temperature anomalies (colored bands) relative to the 1961–1990 climate baseline for Europe (arranged from Ljungqvist et al. [92]). (F) Evolution of the AMO (green line), with an orange band indicating the positive AMO phase (source: Mann et al. [40]). (G) Sunspot number with a 10-year smoothed trend (source: Usoskin et al. [93]). In (D), (F), and (G), the pink vertical line indicates the year of the Tambora eruption in 1815.

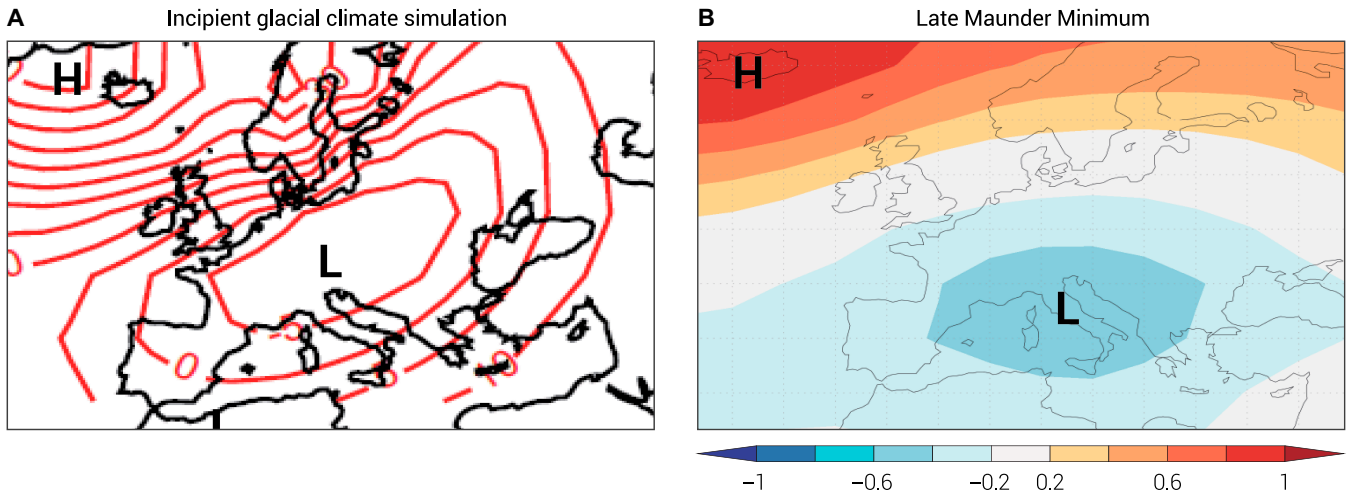

Fig. 7. Climate patterns and pressure variations. (A) Map depicting the difference in the 500-hPa geopotential height (in meters) between the final steady state and the time mean of years 1 to 100 of the synchronously coupled experiment for the incipient glacial climate (final minus initial), adapted from [58]. (B) First EOF (representing 44% of the explained variance) of sea-level pressure during the LMM (1680–1715) across Europe (map obtained from Climate Explorer, http://www.climexp.knmi.nl). "H" represents high pressure, and "L" represents low pressure.

Manara et al. [68] referred to a reduction of the $TCCf_G$ over the central Mediterranean region in decadal time-scale variability from 1951 to 2018, claiming that the origins of this trend are primarily associated with large-scale factors rather than local-scale changes.

Cloud cover responses to forcings

Here, we extended our examination beyond previously explored correlations between precipitation, temperature, and AMO. The Mediterranean climate-type region has witnessed significant warming over the past century, aligning with global trends 69]. The decrease in TCC has contributed to the observed warming trend in recent decades, notably influencing the increase in daily maximum temperatures (T_{max}; Fig. 8). A robust negative correlation ($r < -0.6$) between T_{max} and *TCCf* was evident in the central–western lower Mediterranean and east of the Balkans (Fig. 8A). Conversely, lower correlations were observed in Portugal, Mediterranean France, and central and northern Italy, whereas Turkey showed slightly positive correlation values. Such regional differences toward causality may result from mutual control by (seasonal) synoptic variability [70].

The well-documented phenomenon of increased T_{max} warming associated with widespread reductions in cloud cover often leads to enhanced solar radiation reaching the surface [71]. In the context of ongoing climate change, a decrease in the TCC is expected to amplify the impact of solar radiation, intensifying temperature increases [20]. The dominant warming trend in the Mediterranean basin is attributed to a dual influence: decreasing aerosols and decreasing near-surface soil moisture–temperature feedback [72]. Notably, reduced aerosols may contribute to enhanced rain and snowfall regimes because of the formation of larger cloud droplets with shorter growth times [73]. Meanwhile, models indicating a higher current anticorrelation between TCC and temperature over land suggest a potential future decrease in cloudiness [74]. However, our understanding of how these forcings have influenced cloudiness and surface solar radiation in the North Atlantic over the past 4 decades remains incomplete, particularly regarding the relative importance of different forcing factors [19].

The swift warming of the Arctic is likely a key factor shaping the Mediterranean climate. Noteworthy reductions in Arctic sea ice and spring snow cover have prompted research into dynamic mechanisms linking Arctic amplification to midlatitude weather [75]. A significant positive correlation between Arctic snow cover and *TCCf* was evident over the Mediterranean region (Fig. 7B), with $r \sim 0.5$ over Italy, North Africa, and the central and inland Balkans, whereas lower correlations were observed over Spain, Greece, and Turkey. The influence of Arctic amplification on midlatitude regions involves promoting the negative phase of the Arctic Oscillation and the polar westerly jet stream, resulting in larger meanders [76]. These conditions facilitate the persistence of pressure anomalies, such as the blocking of high pressure in the Ural chain [77]. In this scenario, poleward currents transport Atlantic hydrometeor northward across Western Europe, allowing precipitation from the Atlantic under favorable synoptic conditions. Western Europe's generally flat terrain, without significant mountainous barriers, enables onshore flow to transport warm and moist water vapor and clouds from the Atlantic into the European interior [78].

Implications for future research on cloud–climate interactions

The historical reconstruction of the Mediterranean cloud cover spanning 5 centuries has profound implications for cloud–climate interactions, historical perspectives, and future climate projections. This ambitious effort moves beyond a mere chronological exploration, opening avenues to unravel intricate complexities and offering a new vantage point for comprehending cloud–climate dynamics. Our findings resonate across time, calling for further exploration and reassessment. Whereas conventional models suggest a positive feedback loop-warming enhancing mixing, leading to cloud dissipation (more warming, less clouds, and even more warming; e.g., [20]), recent observations challenge this notion. A trade wind campaign [15] revealed how dynamic cumulus cloud generation can override mixing-induced cloud dissipation, introducing negative feedback and suggesting moderate climate sensitivity [79]. Further research

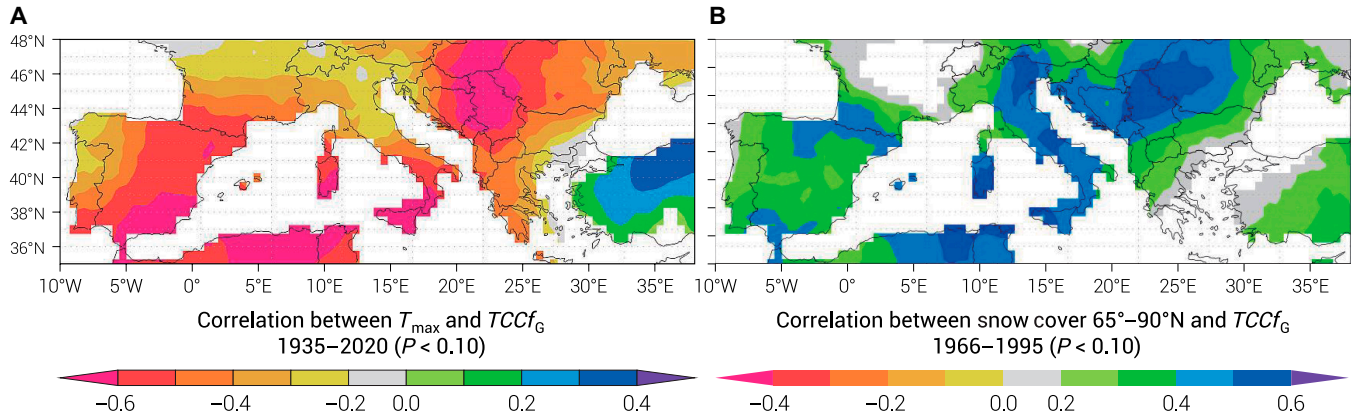

Fig. 8. Correlation analysis of temperature, snow cover, and total cloud fraction. (A) Correlation coefficient between the time series of annual mean maximum temperature (from E-OBS v25.0e Tg Europe analysis 0.25° resolution [94], through http://climexp.knmi.nl/select.cgi?id=b20b645ab14a0cc084e9852606f0eff1&field=ensembles_025_tg_mo) and $TCCf_G$. (B) Correlation between the time series of annual Arctic Circle snow cover (from Rutgers University Global Snow Lab, through http://climexp.knmi.nl/select.cgi?id=b20b645ab14a0cc084e9852606f0eff1&field=rutgers_nhsnow) and $TCCf_G$ field, covering the calibration periods of 1935–2020 and 1965–1995, respectively. $TCCf_G$ data were obtained from CRU TS 4.06.

could focus on constraining circulation responses to warming using observational estimates of static stability through improved low cloud parameterization [5] and targeted model intercomparison studies [80]. This, in turn, can enhance our understanding of equilibrium mechanisms and the nuanced interplay between thermodynamics and cloudiness.

At the core of our analysis lies the unique context of Mediterranean cloudiness, which offers a deeper understanding of cloud–climate interactions and their implications for the future. As we explore the intricate interplay between Mediterranean cloud dynamics and climate factors, it is essential to embed our findings within the broader landscape of global climate research. Historical reconstruction data reveal a consistently negative long-term relationship between temperature and cloud cover, spanning short (interdecadal) and long (from the Medieval era to the present) time scales. Notably, events such as the Tambora eruption had far-reaching global consequences, resonating through the Mediterranean basin and triggering increased cloud cover and enhanced rainfall [81,82]. The nuanced relationship between cloud cover and the 500-hPa geopotential height, as highlighted by studies such as that of Liu et al. [83], indicates decreasing cloud coverage trends over land areas and rising trends in tropical and subtropical oceans between 1980 and 2020.

Understanding the pronounced decline in cloud cover in recent decades involves considering the role of the 500-hPa geopotential height, instability reduction, and tropospheric moisture changes [68,84]. Climate models project a continuous decline in Mediterranean cloud cover throughout the 21st century [85,86], accompanied by a simultaneous increase in solar radiation [87], emphasizing the intertwined influence of ocean-forced processes and thermodynamic mechanisms [88]. Our study invites further exploration into the intricate web of interactions that govern the evolving dynamics between clouds and climate. Through the synthesis of historical insights, observational data, and model projections, we contribute to the ongoing discourse on climate change. Our work emphasizes the significance of understanding Mediterranean cloud dynamics and their wider implications, which are pivotal for comprehending and predicting the complexities of our evolving climate.

Conclusion

Our study undertook a comprehensive effort to reconstruct total annual cloud cover fractions in the Mediterranean region from 1500 to 2022 CE, significantly expanding our understanding of long-term variations in land-based cloud cover. The observed variations exceeded typical background variability, prompting a deeper investigation into the influences of temperature changes—particularly their association with cold air masses through advection—on Mediterranean cloudiness. This enhanced comprehension of the relationships between temperature and cloud cover contributes to the improvement of climate models, thereby enhancing our ability to make more accurate climate predictions.

However, it is essential to acknowledge the inherent limitations of our study, particularly regarding uncertainties prevalent in earlier centuries. The absence of formal sensitivity analysis and reliance on optimized parameters necessitate a cautious interpretation of our findings. Recognizing the potential for refinement through future research endeavors incorporating additional data sources and using refined methodologies may help mitigate uncertainties. A dedicated effort toward a formal sensitivity analysis would provide a more nuanced understanding of the model's robustness and responsiveness to variations in input data, playing a pivotal role in refining our understanding of long-term cloud cover variability in the Mediterranean.

Despite these limitations, our study demonstrated the robustness of the model through calibration and independent validation over different time periods. The incorporation of additional data in future studies promises to further improve the robustness and generalizability of the model, facilitated by optimized parameters of general validity.

The reconstruction of the cloudiness time series contributes to a comprehensive representation of the Mediterranean region, providing valuable insights into long-term variability and advancing our understanding of regional cloud cover dynamics. Moreover, our study's broader implications extend beyond the Mediterranean region. The cloud–climate interactions revealed by our findings transcend geographical boundaries. The implications of our study

extend far beyond the Mediterranean, contributing to a foundational understanding of cloud variability on a global scale. This understanding is imperative for advancing climate science and refining climate models, ultimately leading to more accurate predictions of Earth's future climate scenarios.

In conclusion, our study highlighted the need to improve our understanding of the interactions between climate forces and cloudiness, emphasizing key drivers such as summer precipitation, PDSI, and their interplay with cloudiness and shifts in the AMO. The identified change point in multidecadal variability signaled a subsequent decline in cloudiness since 1818, consistent with concurrent increases in temperature, AMO, solar forcing, and geopotential height of 500 hPa. This intricate link between cloud dynamics and broader climate shifts warrants further investigation to unravel this connection over centuries. Our study bridges historical insights with forward-looking projections, facilitating the evaluation of climate models with real-world observations and providing valuable insights into the nuanced interplay between clouds and climate. By navigating the intricacies of cloud–climate dynamics, our research leads us to a better understanding of the past, present, and possible future of our planet's climate.

Acknowledgment

Funding: We conducted this research as an investigator-driven study without financial support.

Author contributions: N.D. conceptualized and developed the original research design and collected and analyzed historical documentary data. V.K. and G.B. cowrote the article and contributed to the interpretation of the findings. All authors critically reviewed and approved the final manuscript.

Competing interests: The authors declare that they have no competing interests.

Data Availability

All data used in this study are freely available. Artistic representations of cloud phenomena can be found at the following sources: https://en.wikipedia.org/wiki/Wheat_Field_with_Cypresses (Fig. 1A) and https://fr.m.wikipedia.org/wiki/Fichier:Edvard_Munch_-_Train_Smoke_-_Google_Art_Project.jpg (Fig. 1B). Geographical information about the Mediterranean area (Fig. 1A) is accessible from http://www.shadedrelief.com/natural2/globes.html, whereas data on the annual cloud cover fraction over the Mediterranean (Fig. 2B) can be obtained from Climate Explorer (http://climexp.knmi.nl). Correlation coefficients between the summer rainfall time series (Fig. 5A and B) were arranged using data from Climate Explorer (http://climexp.knmi.nl). The evolution of the AMO (Fig. 6H) was derived from Climate Explorer (http://climexp.knmi.nl), and sunspot number data with a 10-year smoothed trend (Fig. 6G) could be accessed at https://www.ncei.noaa.gov/access/paleo-search/study/18475. A map illustrating the PDSI (Fig. 7A and B) was also sourced from Climate Explorer (http://climexp.knmi.nl), as well as sea-level pressure during the LMM (Fig. 7B). The data generated and analyzed in this study are accessible through the data file released with this article (Table S1).

Supplementary Materials

Table S1

References

1. Duveiller G, Filipponi F, Ceglar A, Bojanowski J, Alkama R, Cescatti A. Revealing the widespread potential of forests to increase low level cloud cover. *Nat Commun*. 2021;12(1):4337.
2. Delgado-Bonal A, Marshak A, Yang Y, Holdaway D. Analyzing changes in the complexity of climate in the last four decades using MERRA-2 radiation data. *Sci Rep*. 2020;10:922.
3. Chen Y, Haywood J, Wang Y, Malavelle F, Jordan G, Partridge D, Fieldsend J, De Leeuw J, Schmidt A, Cho N, et al. Machine learning reveals climate forcing from aerosols is dominated by increased cloud cover. *Nat Geosci*. 2022;15(8):609–614.
4. Liu F, Mao F, Rosenfeld D, Pan Z, Zang L, Zhu Y, Yin J, Gong W. Opposing comparable large effects of fine aerosols and coarse sea spray on marine warm clouds. *Commun Earth Environ*. 2022;3(1):232.
5. Kang SM, Ceppi P, Yu Y, Kang I-S. Recent global climate feedback controlled by Southern Ocean cooling. *Nat Geosci*. 2023;16(9):775–780.
6. Barney SA, Lewis WJ, Beach JA, Berghof O. *The etymologies of Isidore of Seville*. Cambridge: Cambridge University Press; 2006.
7. Bony S, Stevens B, Frierson D, Jakob C, Kageyama M, Pincus R, Shepherd TG, Sherwood SC, Siebesma AP, Sobel AH, et al. Clouds, circulation and climate sensitivity. *Nat Geosci*. 2015;8(4):261–268.
8. Vaideanu P, Dima M, Voiculescu M. Atlantic Multidecadal Oscillation footprint on global high cloud cover. *Theor Appl Climatol*. 2018;134(6):1245–1256.
9. Mülmenstädt J, Salzmann M, Kay JE, Zelinka MD, Ma P-L, Nam C, Kretzschmar J, Hörnig S, Quaas J. An underestimated negative cloud feedback from cloud lifetime changes. *Nat Clim Chang*. 2021;11(6):508–513.
10. Kumar V, Dhaka SK, Hitchman MH, Yoden S. The influence of solar-modulated regional circulations and galactic cosmic rays on global cloud distribution. *Sci Rep*. 2023;13(1):3707.
11. Watson-Parris D, Smith CJ. Large uncertainty in future warming due to aerosol forcing. *Nat Clim Chang*. 2022;12(12):1111–1113.
12. Albright AL, Huybers P. Paintings by Turner and Monet depict trends in 19th century air pollution. *Proc Natl Acad Sci USA*. 2023;120(6):Article e2219118120.
13. Wang W, Zeng X, Liu X, An W, Zhang L. Temporal evolution of the influence of atmospheric circulation on regional cloud cover as revealed by tree-ring $\delta^{18}O$ in southwestern China. *Glob Planet Chang*. 2022;208(12):Article 103690.
14. Yuan T, Oreopoulos L, Platnick SE, Meyer K. Observations of local positive low cloud feedback patterns and their role in internal variability and climate sensitivity. *Geophys Res Lett*. 2018;45(4):4438–4445.
15. Vogel R, Albright AL, Vial J, George G, Stevens B, Bony S. Strong cloud–circulation coupling explains weak trade cumulus feedback. *Nature*. 2022;612(7941):696–700.
16. Kalimeris A, Founda D. Inter-annual and inter-decadal variability modes of the Athens total cloud cover. *Int J Climatol*. 2018;38(679):4667–4686.
17. Clement A, Bellomo K, Murphy LN, Cane MA, Mauritsen T, Rädel G, Stevens B. The Atlantic Multidecadal Oscillation without a role for ocean circulation. *Science*. 2015;350(6258):320–324.
18. Martens B, Waegeman W, Dorigo WA, Verhoest NEC, Miralles DG. Terrestrial evaporation response to modes of climate variability. *Npj Clim Atmosp Science*. 2018;1(1):43.

19. Dong B, Sutton RT, Wilcox LJ. Decadal trends in surface solar radiation and cloud cover over the North Atlantic sector during the last four decades: Drivers and physical processes. *Clim Dyn*. 2023;60(7-8):2533–2546.
20. Mendoza V, Pazos M, Garduño R, Mendoza B. Thermodynamics of climate change between cloud cover, atmospheric temperature and humidity. *Sci Rep*. 2021;11(1):21244.
21. Ceppi P, Nowack P. Observational evidence that cloud feedback amplifies global warming. *Proc Natl Acad Sci USA*. 2021;118(30):Article e2026290118.
22. Pliemon T, Foelsche U, Rohr C, Pfister C. Subdaily meteorological measurements of temperature, direction of the movement of the clouds, and cloud cover in the Late Maunder Minimum by Louis Morin in Paris. *Clim Past*. 2022;18(7):1685–1707.
23. Brázdil R, Cernusak T, Reznickova L. *The weather and climate in the region of Olomouc, Czech Republic, based on premonstratensian diaries kept by the Hradisko Monastery and Svaty Kopecek Priory, 1693-1783,* Brno: Masaryk University; 2011.
24. Sanchez-Lorenzo A, Calbo J, Wild M. Increasing cloud cover in the 20th century: Review and new findings in Spain. *Clim Past*. 2012;8(8):1199–1212.
25. Teuling A, Taylor C, Meirink J, Melsen LA, Miralles DG, van Heerwaarden CC, Vautard R, Stegehuis AI, Nabuurs G-J, Vilà-Guerau de Arellano J. Observational evidence for cloud cover enhancement over western European forests. *Nat Commun*. 2017;8(1):14065.
26. Bartoszek K, Łachowski W, Matuszko D. The increase in the proportion of impervious surfaces and changes in air temperature, relative humidity and cloud cover in Poland. *Quaest Geograp*. 2023;42(1):25–41.
27. Sanchez-Lorenzo A, Enriquez-Alonso A, Calbó J, González J-A, Wild M, Folini D, Norris JR, Vicente-Serrano SM, Vicente-Serrano SM. Fewer clouds in the Mediterranean: Consistency of observations and climate simulations. *Sci Rep*. 2017;7(1):41475.
28. Tzallas V, Hatzianastassiou N, Benas N, Meirink JF, Matsoukas C, Stackhouse P Jr, Vardavas I. Evaluation of CLARA-A2 and ISCCP-H cloud cover climate data records over Europe with ECA&D ground-based measurements. *Remote Sens*. 2019;11(212):212.
29. Aparicio AJP, Carrasco VMS, Montero-Martín J, Sanchez-Lorenzo A, Costa MJ, Antón M. Analysis of sunshine duration and cloud cover trends in Lisbon for the period 1890–2018. *Atmos Res*. 2023;290(2):Article 106804.
30. Founda D, Nastos PT, Pierros F, Kalimeris A. Historical observations of cloudiness (1882−2012) over a large urban area of the eastern Mediterranean (Athens). *Theor Appl Climatol*. 2019;137(11):283–295.
31. Matuszko D, Weglarczyk S. Effect of cloudiness on long-term variability in air temperature in Krakow. *Int J Climatol*. 2014;34(1):145–154.
32. Todaro V, D'Oria M, Secci D, Zanini A, Tanda MG. Climate change over the Mediterranean region: Local temperature and precipitation variations at five pilot sites. *Water*. 2022;14(16):2499.
33. Gregory JM, Andrews T. Variation in climate sensitivity and feedback parameters during the historical period. *Geophys Res Lett*. 2016;43(8):3911–3920.
34. Lionello P, Malanotte-Rizzoli P, Boscolo R, Alpert P, Artale V, Li L, Luterbacher J, May W, Trigo R, Tsimplis M, et al. The Mediterranean climate: An overview of the main characteristics and issues. In: Lionello P, Malanotte-Rizzoli P, Boscolo R, editors. *Mediterranean climate variability* Amsterdam: Elsevier; 2006. p. 1–26.
35. Ioannidis E, Lolis CJ, Papadimas CD, Hatzianastassiou N, Bartzokas A. On the intra-annual variation of cloudiness over the Mediterranean region. *Atmoshp Res*. 2018;208: 246–256.
36. Lolis CJ, Kotsias G, Bartzokas A. Objective definition of climatologically homogeneous areas in the Southern Balkans based on the ERA5 data set. *Climate*. 2018;6(4):96.
37. Pauling A, Luterbacher J, Casty C, Wanner H. Five hundred years of gridded high-resolution precipitation reconstructions over Europe and the connection to large-scale circulation. *Clim Dyn*. 2006;26(4):387–405.
38. Luterbacher J, Dietrich D, Xoplaki E, Grosjean M, Wanner H. European seasonal and annual temperature variability, trends, and extremes since 1500. *Science*. 2004;303(5663):1499.
39. Cook ER, Seager R, Kushnir Y, Briffa KR, Büntgen U, Frank D, Krusic PJ, Tegal W, van der Schrier G, Andreu-Hayles L, et al. Old World megadroughts and pluvials during the Common Era. *Sci Adv*. 2015;2015(1):Article e1500561.
40. Mann ME, Zhang Z, Rutherford S, Bradley RS, Hughes MK, Shindell D, Ammann C, Greg F, Ni F. Global signatures and dynamical origins of the Little Ice Age and Medieval Climate Anomaly. *Science*. 2009;326(5957):1256–1260.
41. Harris I, Osborn TJ, Jones P, Lister D. Version 4 of the CRU TS monthly high-resolution gridded multivariate climate dataset. *Sci Data*. 2020;7(1):109.
42. Štěpánek P. *AnClim - Software for time series analysis*. Brno: Masaryk University; 2005.
43. Wilby RL, Hay LE, Leavesley GH. A comparison of downscaled and raw GCM output: Implications for climate change scenarios in the San Juan River basin, Colorado. *J Hydrol*. 1999;225(1-2):67–91.
44. Groisman P, Bradley RS, Sun B. The relationship of cloud cover to near-surface temperature and humidity: Comparison of GCM simulations with empirical data. *J Clim*. 2000;13(11):1858–1878.
45. Duhan D, Pandey A, Gahalaut KPS, Pandey RP. Spatial and temporal variability in maximum, minimum and mean air temperatures at Madhya Pradesh in Central India. *Compt Rendus Geosci*. 2013;345(1):3–21.
46. Dong B, Sutton RT, Shaffrey L. Understanding the rapid summer warming and changes in temperature extremes since the mid-1990s over Western Europe. *Clim Dyn*. 2017;48(5-6):1537–1554.
47. Matuszko D, Bartoszek K, Soroka J. Long-term variability of cloud cover in Poland (1971–2020). *Atmos Res*. 2022;268(5939):Article 106028.
48. Huntington TG. Evidence for intensification of the global water cycle: Review and synthesis. *J Hydrol*. 2006;319:83–95.
49. Mishra AK. Investigating changes in cloud cover using the long-term record of precipitation extremes. *Meteorol Appl*. 2019;26:108–116.
50. Cox DTC, Maclean IMD, Gardner AS, Gaston KJ. Global variation in diurnal asymmetry in temperature, cloud cover, specific humidity and precipitation and its association with leaf area index. *Glob Chang Biol*. 2020;26:7099–7111.
51. Richards F, Arkin P. On the relationship between satellite-observed cloud cover and precipitation. *Mon Weather Rev*. 1981;109:1081–1093.

52. Yue S, Wang B, Yang K, Xie Z, Lu H, He J. Mechanisms of the decadal variability of monsoon rainfall in the southern Tibetan plateau. *Environ Res Lett*. 2020;16:Article 014011.
53. Zhu S, Chen H, Dong X, Wei J. Influence of persistence and oceanic forcing on global soil moisture predictability. *Clim Dyn*. 2020;54(7):3375–3385.
54. Semenov VA, Latif M, Dommenget D, Keenlyside NS, Strehz A, Martin T, Park W. The impact of North Atlantic–Arctic multidecadal variability on Northern Hemisphere surface air temperature. *J Clim*. 2010;23(21):5668–5677.
55. Markonis Y, Hanel M, Máca P, Kyselý J, Cook ER. Persistent multi-scale fluctuations shift European hydroclimate to its millennial boundaries. *Nat Commun*. 2018;9(1):1767.
56. Fagan B. *The Little Ice Age: How climate made history 1300-1850*. New York: Basic Book; 2000.
57. Benestad RE, Mezghani A, Lutz J, Dobler A, Parding KM, Landgren OA. Various ways of using empirical orthogonal functions for climate model evaluation. *Geosci Model Dev*. 2023;16(10):2899–2913.
58. Gregory JM, Browne OJH, Payne AJ, Ridley JK, Rutt IC. Modelling large-scale ice-sheet–climate interactions following glacial inception. *Clim Past*. 2012;8:1565–1580.
59. Trigo RM, Trigo IF, DaCamara CC, Osborn TJ. Climate impact of the European winter blocking episodes from the NCEP/NCAR reanalyses. *Clim Dyn*. 2004;23(1):17–28.
60. Cook BI, Smerdon JE, Cook ER, Williams AP, Anchukaitis KJ, Mankin JS, Allen K, Andreu-Hayles L, Ault TR, Belmecheri S, et al. 2022 Megadroughts in the Common Era and the Anthropocene. *Nat Rev Earth Environ*. 2022;3(11):741–757.
61. Barriendos M, Llasat MC. The case of the 'Maldá' anomaly in the Western Mediterranean Basin (AD 1760–1800): An example of a strong climatic variability. *Clim Chang*. 2003;61(1):191–216.
62. Diodato N, Bellocchi G. Historical perspective of drought response in Mediterranean Italy. *Clim Res*. 2011;49(3):189–200.
63. Young GHF, Gagen MH, Loader NJ, McCarroll D, Grudd H, Jalkanen R, Kirchhefer A, Robertson I. Cloud cover feedback moderates Fennoscandian summer temperature changes over the past 1,000 years. *Geophys Res Lett*. 2019;46(5):2811–2819.
64. Knudsen MF, Jacobsen BH, Seidenkrantz M-S, Olsen J. Evidence for external forcing of the Atlantic Multidecadal Oscillation of the Little ice Age. *Nat Commun*. 2014;5(1):3323.
65. Burić D, Stanojević G. Trends and possible causes of cloudiness variability in Montenegro in the period 1961−2017. *Clim Res*. 2020;81:187–205.
66. Qian Y, Kaiser DP, Leung LR, Xu M. More frequent cloud-free sky and less surface solar radiation in China from 1955 to 2000. *Geophys Res Lett*. 2006;33(1):L01812.
67. Sfîcă L, Beck C, Nita A-I, Voiculescu M, Birsan M-V, Philipp A. Cloud cover changes driven by atmospheric circulation in Europe during the last decades. *Int J Climatol*. 2021;41:E2211–E2230.
68. Manara V, Brunetti M, Wild M, Maugeri M. Variability and trends of the total cloud cover over Italy (1951–2018). *Atmos Res*. 2023;285:Article 106625.
69. Cramer W, Guiot J, Fader M, Garrabou J, Gattuso J-P, Iglesias A, Lange MA, Lionello P, Llasat MC, Paz S, et al. Climate change and interconnected risks to sustainable development in the Mediterranean. *Nat Clim Chang*. 2018;8(3-4):972–980.
70. Warren SG, Eastman RM, Hahn CJ. A survey of changes in cloud cover and cloud types over land from surface observations, 1971-1996. *J Clim*. 2007;20(4):717–738.
71. Zhong Z, He B, Chen HW, Chen D, Zhou T, Dong W, Xiao C, Xie SP, Song X, Guo L, et al. Reversed asymmetric warming of sub-diurnal temperature over land during recent decades. *Nat Commun*. 2023;14(1):7189.
72. Urdiales-Flores D, Zittis G, Hadjinicolaou P, Osipov S, Klingmüller K, Mihalopoulos N, Kanakidou M, Economou T, Lelieveld J. Drivers of accelerated warming in Mediterranean climate-type regions. *Npj Clim Atmosp Science*. 2023;6(1):97.
73. Shepherd JM. A review of current investigations of urban induced rainfall and recommendations for the future. *Earth Interact*. 2005;9(12):1–27.
74. Boé J, Terray L. Land-sea contrast, soil-atmosphere and cloud-temperature interactions: Interplays and roles in future summer European climate change. *Clim Dyn*. 2014;42(3-4):683–699.
75. Cohen J, Screen J, Furtado J, Barlow M, Whittleston D, Coumou D, Francis J, Dethloff K, Entekhabi D, Overland J, et al. Recent Arctic amplification and extreme mid-latitude weather. *Nat Geosci*. 2014;7(9):627–637.
76. Zhang X, He J, Zhang J, Polyakov I, Gerdes R, Inoue J, Wu P. Enhanced poleward moisture transport and amplified northern high-latitude wetting trend. *Nat Clim Chang*. 2013;3(1):47–51.
77. Francis JA, Vavrus SJ. Evidence linking Arctic amplification to extreme weather in mid-latitudes. *Geophys Res Lett*. 2012;39(6):L06801.
78. Cheng J, You Q, Zhou Y, Cai M, Pepin N, Chen D, AghaKouchak A, Kang S, Li M. Increasing cloud water resource in a warming world. *Environ Res Lett*. 2021;16:Article 124067.
79. Cesana GV, Del Genio AD. Observational constraint on cloud feedbacks suggests moderate climate sensitivity. *Nat Clim Chang*. 2021;11(3):213–218.
80. Schiro KA, Su H, Ahmed F, Daj N, Singer CE, Gentine P, Elsaesser GS, Jiang JH, Choi Y-S, Neelin JD, et al. Model spread in tropical low cloud feedback tied to overturning circulation response to warming. *Nat Commun*. 2022;13(1):7119.
81. Wood GD. *Tambora: the eruption that changed the world*. Princeton: Princeton University Press; 2014.
82. Brönnimann S, Krämer D. *Tambora and the "Year Without a Summer" of 1816. A perspective on Earth and human systems science*. Bern: Geographica Bernensia; 2016.
83. Liu H, Koren I, Altaratz O, Chekroun MD. Opposing trends of cloud coverage over land and ocean under global warming. *Atmosp Chem Phys*. 2023;23(11):6559–6569.
84. Khodayar S, Caldas-Alvarez A. Seasonal heavy precipitation sensitivity to moisture corrections in the western Mediterranean across resolutions. *Atmos Res*. 2022;280(D14):Article 106429.
85. Enriquez-Alonso A, Sanchez-Lorenzo A, Calbó J, González JA, Norris J. Cloud cover climatologies in the Mediterranean obtained from satellites, surface observations, reanalyses, and CMIP5 simulations: Validation and future scenarios. *Climatic Dynamics*. 2016;47(1):249–269.
86. Wild M, Folini D, Henschel F, Fischer N, Müller B. Projections of long-term changes in solar radiation based on CMIP5 climate models and their influence on energy yields of photovoltaic systems. *Sol Energy*. 2015;116:12–24.
87. Zhou C, Zelinka MD, Klein SA. Impact of decadal cloud variations on the Earth's energy budget. *Nat Geosci*. 2016;9(12):871–874.
88. Qasmi S, Sanchez-Gomez E, Ruprich-Robert Y, Boé J, Cassou C. Modulation of the occurrence of heatwaves over

the Euro-Mediterranean region by the intensity of the Atlantic multidecadal variability. *J Clim*. 2021;34(3):1099–1114.
89. Vincent DP, Gogh V. *I miei quadri raccontati da me.* Rome: Donzelli; 2017 (in Italian).
90. Schneider U, Becker A, Finger P, Rustemeier E, Ziese M. *GPCC Full data monthly product version 2020 at 0.25°: Monthly land-surface precipitation from rain-gauges built on GTS-based and historical data.* Berlin: Federal Ministry for Digital and Transport; 2020.
91. Alexandersson H, Moberg A. Homogenization of Swedish temperature data. Part I: Homogeneity test for linear trends. *Int J Climatol*. 1997;17(1):25–34.
92. Ljungqvist FC, Seim A, Krusic PJ, González-Rouco JF, Werner JP, Cook ER, Zorita E, Luterbacher J, Xoplaki E, Destouni G, et al. European warm-season temperature and hydroclimate since 850 CE. *Environ Res Lett*. 2019;14(8):Article 084015.
93. Usoskin IG, Hulot G, Gallet Y, Roth R, Licht A, Joos F, Kovaltsov GA, Thébault E, Khokhlov A. Evidence for distinct modes of solar activity. *Astron Astrophys*. 2014;562:L10.
94. Cornes R, van der Schrier G, van den Besselaar EJM, Jones PD. An ensemble version of the E-OBS temperature and precipitation datasets. *J Geophys Res*. 2018;123(17):9391–9409.